ADVANCED MATERIALS
www.advmat.de

Extreme-Angle Silicon Infrared Optics Enabled by Streamlined Surfaces

*Fei Zhang, Mingbo Pu, Xiong Li, Xiaoliang Ma, Yinghui Guo, Ping Gao, Honglin Yu, Min Gu, and Xiangang Luo**

Infrared optical systems are indispensable in almost all domains of society, but their performances are often restricted by bulky size, small field of view, large thermal sensitivity, high fabrication cost, etc. Here, based on the concept of catenary optics, a novel isophase streamline optimization approach is leveraged to design silicon complementary metal–oxide–semiconductor (CMOS)-compatible metasurfaces with broadband, wide-angle, and high-efficiency performances, which breaks through the glass ceiling of traditional optical technologies. By using the truly local geometric phase, a maximum diffraction efficiency approaching 100% is obtained in ultrawide spectral and angular ranges. Somewhat surprising results are shown in that wide-angle diffraction-limited imaging and laser beam steering can be realized with a record field of view up to 178°. This methodology is scalable to the entire optical band and other materials, enabling unprecedented compact infrared systems for surveillance, unmanned vehicles, medical science, etc.

1. Introduction

As extensions of the ability of the human eye, infrared imaging and lidar techniques have found many important applications in night vision, surveillance, unmanned vehicles, medical science, and so forth.[1] For instance, thermal imagers have been widely employed for rapid temperature measurement of the public, making important contributions to the fight against infectious diseases such as COVID-19. However, traditional infrared optics often suffers from several long-standing challenges, including bulky size, large thermal sensitivity, small field of view (FOV), high fabrication cost, and few available materials. On the one hand, the change in refractive index with temperature is significantly larger for most infrared materials than for normal optical glasses, resulting in much larger thermal focus shifts. The lack of high-quality infrared materials has made the design of infrared optical systems much more complex. On the other hand, according to the aberration theory, the complexity of optical systems, including the number of optical elements and surface curvatures, will be further increased if high-resolution imaging at large FOV is required.[2,3]

In the past decade, optical metasurfaces consisting of subwavelength elements have been extensively explored to engineer light-matter interactions in a virtually planar surface, offering unusual electromagnetic properties not available in traditional bulky optical elements.[4,5] Many exotic phenomena and applications have been realized, such as photonic spin–orbit interactions,[6–8] achromatic wavefront shaping,[9,10] multidimensional full-color holography,[11,12] invisibility cloaking,[13,14] image differentiation,[15,16] near-field wave control,[17–19] and many others.[20–22] Especially, multistate switching of photonic angular momentum coupling, namely, symmetric, asymmetric, and none coupling, have been experimentally demonstrated at different crystallization levels of phase-change metasurfaces.[23] The subwavelength thickness of metasurfaces makes the absorption loss therein much smaller than bulky optical elements. For example, as the material basis of microelectronic technology, silicon is not considered for the long-wave infrared region because of its high absorption in the region of 8–14 μm. With the advent of metasurface technologies, all-silicon functional optical elements become possible,[6,24] providing new opportunities for the integration of optical and electronic systems in a single platform. More interestingly, in metalenses based on geometric phase or so-called photonic spin–orbit interactions,[25] the phase gradient is only dependent on the geometric shapes, thus thermal sensitivity of refractive index could be ignored through proper designs.

Dr. F. Zhang, Prof. M. Pu, Prof. X. Li, Prof. X. Ma, Prof. Y. Guo, Prof. P. Gao, Prof. X. Luo
State Key Laboratory of Optical Technologies on Nano-Fabrication and Micro-Engineering
Institute of Optics and Electronics
Chinese Academy of Sciences
Chengdu 610209, China
E-mail: lxg@ioe.ac.cn
Dr. F. Zhang, Prof. H. Yu
Key Laboratory of Optoelectronic Technology and System
Ministry of Education
Chongqing University
Chongqing 400030, China
Prof. M. Pu, Prof. X. Li, Prof. X. Ma, Prof. Y. Guo, Prof. P. Gao, Prof. X. Luo
School of Optoelectronics
University of Chinese Academy of Sciences
Beijing 100049, China
Prof. M. Gu
Centre for Artificial-Intelligence Nanophotonics
School of Optical-Electrical and Computer Engineering
University of Shanghai for Science and Technology
Shanghai 201210, China
The ORCID identification number(s) for the author(s) of this article can be found under https://doi.org/10.1002/adma.202008157.

DOI: 10.1002/adma.202008157

The combination of novel functionalities and complementary metal–oxide–semiconductor (CMOS)-compatible fabrication processes in optical metasurfaces has enabled a new era of optical engineering that not available with traditional technologies.[26–30] However, practical metasurfaces must simultaneously take account of energy efficiency, angular range, and spectral bandwidth, which are three main indicators that determine the imaging quality, resolution, and FOV.[2,31] According to fundamental diffraction theory,[32] however, it is of great challenge to efficiently bend light at a large deflection angle owing to insufficient phase sampling over a limited space. Finely sampling the phase distribution would prefer a smaller element spacing, which is, however, limited by the poor fabrication feasibility and electromagnetic coupling between adjacent elements.[31,33] Waveguide-type and resonant nanostructures such as high-refractive-index nanopillars with strong transversal confinement may enable a good balance between the sampling and coupling effects, but they come at the cost of narrower spectral bandwidth.[31,34]

To overcome the limitation of discrete metasurfaces, some novel geometries such as metallic catenary structures and dielectric nanoarc structures[25,35–37] have been proposed to generate continuous phase profiles in a wide spectral band. However, their phase and amplitude responses are far from perfect, resulting in reduced efficiency and obvious spurious diffraction orders. Recently, it has been demonstrated that topology optimization can improve the performance of continuous structures.[38–40] Nevertheless, limited by the requirement of extensive numerical simulations, most of the topology-optimized devices are confined to either periodic structures or small-area devices. It is still extremely time-consuming for the design of large-area metasurfaces with 2D phase profiles. Consequently, there are no known metasurfaces that simultaneously offer broadband, high-efficiency, and wide-angle wavefront control.[31]

Here, based on the concept of catenary optics, we report a general and non-time-consuming design strategy of isophase streamline optimization for all-dielectric optical metasurfaces with broadband, high-efficiency, and ultrawide-angle wavefront control ability. Owing to the ingenious optimization on continuous streamlined shapes, spurious diffraction orders are nullified in the near and long-wave infrared region for almost any angle of incidence. Ultrawide-angle (178°) diffraction-limited imaging was realized using only a single metasurface, showing unprecedented imaging performance regarding the efficiency and angular range. Meanwhile, extreme-angle (>170°) laser beam scanning was also demonstrated by shifting a spot source on the focal plane of the wide-angle streamlined metalens, providing a promising candidate for lightweight and wide-angle lidar systems. Since silicon flat optical systems are compatible with both infrared imaging and CMOS technologies, our results may open a door for the widespread applications of flat infrared optical systems in many areas.

2. Concept of Streamlined Metasurfaces

The heart of silicon wide-angle flat metalens is the local control of phase delay in a wide range of wavelengths and angles of incidence. In general, the phase delay introduced by optical subwavelength structures can be mainly categorized into the propagation phase and geometric phase (also referred to as the Pancharatnam–Berry phase).[27] The propagation phase is usually related to the refractive index, wavelength, and incident angle, so it is hard to simultaneously realize broadband, high-efficiency, wide-angle, and temperature-independent wavefront control.[31] In contrast, the geometric phase carried by the spin-reversed circularly polarized (CP) component depends only on the spin of incident CP light and the orientation of anisotropic structures, thus it is intrinsically dispersion-free and refraction-index-independent.[25] Although the diffraction efficiency of geometric phase is related to the polarization conversion and dependent on the wavelength, a proper dispersion engineering of the material and structural dispersion can eliminate this in a broad wavelength range.[3,28]

According to the Jones matrix formalism, streamlined anisotropic structures comprising space-variant half-wave plates can yield an angle-dependent geometric phase distribution, $-2\sigma\xi(x, y)$, where $\sigma = \pm 1$ denotes left- and right-handed CP light, while $\xi(x, y)$ indicates the inclination angle between the x-axis and the main axis.[25] Here, streamlines refer to a family of curves that are instantaneously tangent to one vector field. Owing to the continuous streamlines, the diffraction efficiency can be maximized to obtain a near-perfect wavefront. **Figure 1** shows an example of the streamlined profile of a metalens that focuses left-handed CP incidence into a tight spot. The time-reversed electric field (blue arrows) on the xy-plane ($z = 0$) can be obtained by analyzing the radiation from a right-handed CP point source that is placed at a distance z_0 along the z-axis and can be approximately written as $E_x = \exp[i\phi(x, y)]$ and $E_y = i\exp[i\phi(x, y)]$, where $\phi(x, y) = -k(x^2 + y^2 + z_0^2)^{1/2}$ and $k = 2\pi/\lambda$. Such a field could be generated by illuminating a left-handed CP light onto a half-wave plate with spatially variant anisotropic axes. The conversion process can be written as[25]

$$\begin{bmatrix} e^{i\phi(x,y)} \\ ie^{i\phi(x,y)} \end{bmatrix} = \begin{bmatrix} \cos^2\xi(x,y)-\sin^2\xi(x,y) & 2\sin\xi(x,y)\cos\xi(x,y) \\ 2\sin\xi(x,y)\cos\xi(x,y) & \sin^2\xi(x,y)-\cos^2\xi(x,y) \end{bmatrix} \begin{bmatrix} 1 \\ -i \end{bmatrix} \tag{1}$$

where $\xi(x, y) = -\phi(x, y)/2$ is the space-variant inclination angle. Mathematically, the continuous main axes could be seen as the streamlines of a new vector field defined by $U_x = \exp[i\phi(x, y)/2]$ and $U_y = i\exp[i\phi(x, y)/2]$, which is illustrated as orange arrows in the top right of Figure 1. Then, the local slope of such an auxiliary vectorial field is determined by a differential equation

$$\frac{\mathrm{d}y}{\mathrm{d}x} = \frac{\mathrm{Re}(U_y)}{\mathrm{Re}(U_x)} = -\tan\left[\phi(x,y)/2\right] \tag{2}$$

Subsequently, the coordinate of the streamline can be obtained by numerical integration as

$$\begin{aligned} x_{m+1} &= x_m + \cos\left[\phi(x_m, y_m)/2\right]\mathrm{d}r \\ y_{m+1} &= y_m - \sin\left[\phi(x_m, y_m)/2\right]\mathrm{d}r \end{aligned} \tag{3}$$

where dr indicates the integral step length and should be small enough. By appropriately choosing the starting/end

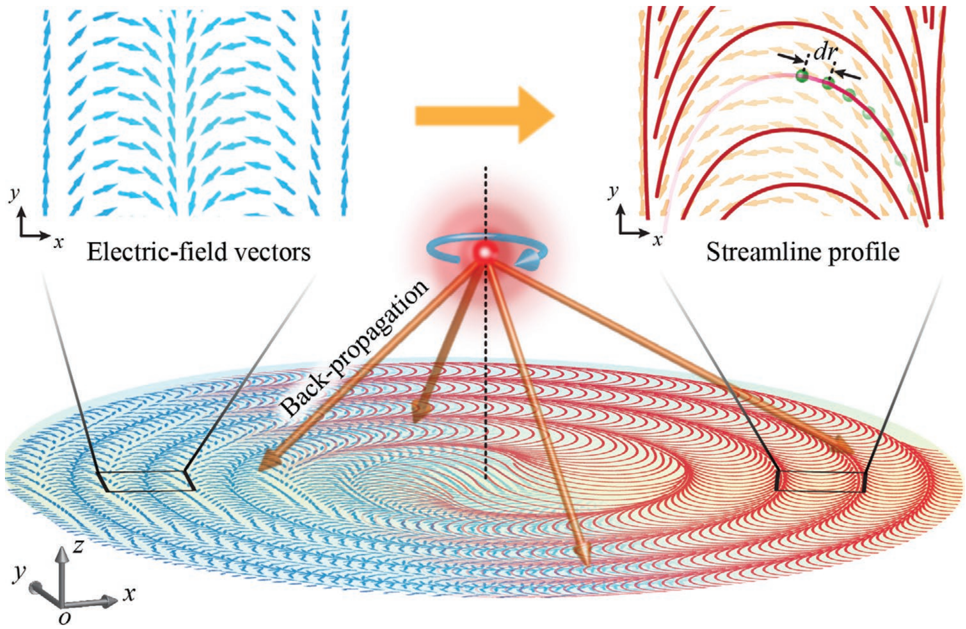

Figure 1. Concept illustration of the streamlined metalens. The time-reversed electric fields (blue arrows) are obtained by the radiation of a CP point source and could be generated by a half-wave plate with spatially variant anisotropic axes. The red streamline is obtained by the trajectory of the vectorial field (orange arrows) formed by spatially variant anisotropic axes mentioned above.

points, the whole plane can be filled with streamlines with desired density.

After obtaining the streamlines, one needs to convert them into solid shapes. To overcome the ohmic loss of metallic structures, dielectric materials are preferred.[25,35,36] Among many different dielectric materials, silicon may be an ideal choice because of its high refractive index and CMOS-compatible fabrication. The high refractive index of silicon is helpful for the realization of truly local phase modulation and the improvement of the diffraction efficiency at large angles,[41,42] because high-index dielectric structures can behave as a waveguide that confines the light throughout the structure. Besides, the dispersion of silicon-based form-birefringence enables broadband and high-efficiency polarization conversion.[43]

By combining the geometric-phase-determined streamlines and silicon dielectric structures, it is possible to construct novel metasurfaces with broadband and high efficiencies over a wide angular range. However, since local periods of these streamlines are not equal, there would be a parasitic propagation phase gradient that is not required. Considering a single anisotropic optical element with an orientation angle of ξ and phase shifts of $\beta \pm \pi/2$ for two orthogonal polarizations, the spin-reversed component carries not only the spin-dependent geometric phase $-2\sigma\xi$ but also the spin-independent propagation phase β.[44] Since such a parasitic phase gradient would enhance spurious diffraction orders, we developed an isophase streamline optimization strategy to realize pure geometric phase modulation.

3. Isophase Streamline Optimization Strategy

Without loss of the generality, we use a grating-like beam deflector to illustrate the principle of isophase streamline optimization. The periodic structures enable us to quantify the efficiency and bandwidth more accurately with the Floquet theorem. As depicted in **Figure 2**a, an optimized streamlined metasurface (OSM) is designed to bend light at a wavelength of 10.6 µm to −45° along the x-direction. The required phase distribution should be $2\pi x/\Lambda$, where $\Lambda = 10.6/\sin(45°)$ is the horizontal period of the OSM. The streamline trajectory can be easily calculated to be a "catenary of equal strength": $y = \Lambda/\pi \cdot \ln|\sec(\pi x/\Lambda)|$.[25] Catenary optics has been a new and exciting direction of research in subwavelength optics and electromagnetics, whose history, theories, and applications are introduced in a recent review.[45]

To illustrate the influence of the parasitic phase in this space-varying structure, it is helpful to consider the influence of the local period on the propagation phase shift. As shown in the inset of Figure 2a, the local period p and local width w_1 are defined along the normal line of the streamlines. The key to realizing the isophase streamline optimization is to spatially vary w_1 by resorting to a database of the local period, width, and propagation phase. Here the isophase refers to an equal-propagation-phase line in the parameter space of ordinary 1D gratings (see Section S1 in the Supporting Information for details). Figure 2b shows the local width of the streamlined structure along the x-direction corresponding to a constant propagation phase distribution. As shown by the orange dots in Figure 2c, the simulated phase distribution of the OSM at the design wavelength agrees well with the ideal one (green line). By contrast, there is an additional parasitic phase (magenta curve) accompanied by the geometric phase for a normal streamlined metasurface (NSM).[25]

Figure 2d displays scanning electron microscopy (SEM) images of a fabricated OSM. From the simulated electric field distribution of real (E_x) displayed in Figure 2e under

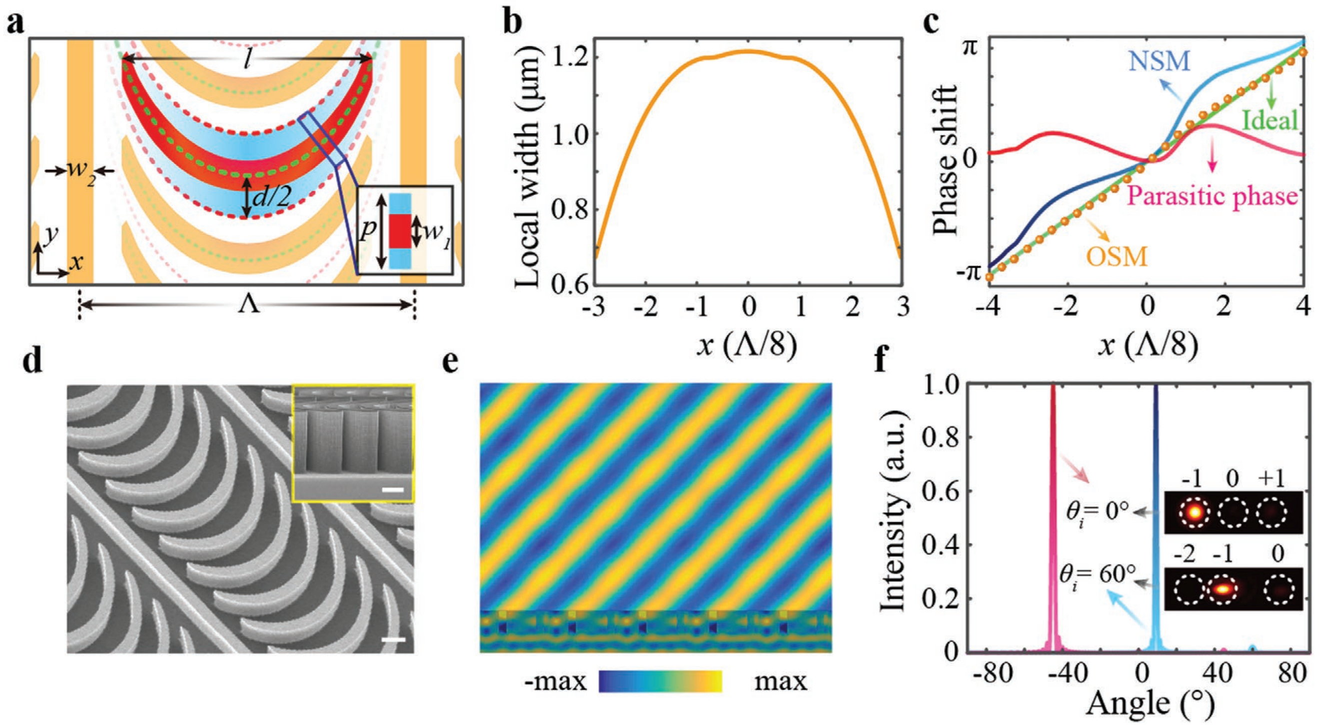

Figure 2. Characterization of OSMs. a) Schematic illustration of an OSM. The dashed curves are an array of streamlines with an interval of $d/2$ along the y-direction (d = 3.3 µm). The streamlines are truncated ($l = 0.75\Lambda$) to guarantee the feasibility of fabrication. Vertical structures with a width of w_2 are added in truncated regions to increase the phase continuity and amplitude uniformity. b) Local width profile of the streamlined structure in the OSM with $\Lambda = 10.6/\sin(45°)$ µm and w_2 = 1.18 µm. c) Simulated total phase profiles of the OSM (orange dots) and NSM (blue curve) as well as the parasitic phase gradient of the NSM (magenta curve) along the x-direction under normal incidence. The parasitic phase of the NSM is derived from its total phase minus the geometric phase (green line). d) SEM images of the OSM. The inset shows its sectional drawing. Scale bar: 2 µm. e) Simulated real (E_x) distribution of the OSM. The darkened strip denotes the structural region. f) Far-field intensity profiles at normal and oblique incidence. The insets represent corresponding measured diffraction patterns.

normal incidence, it can be seen that almost all the energy of transmitted light is directed into the first order, which is further validated by the simulated far-field intensity profiles and measured diffraction patterns (Figure 2f). The measured-first-order diffraction efficiencies are 96.6% and 92.6% for two incident angles of 0° and 60°, respectively, being very close to the simulated results (98.4% and 95.7%). The diffraction/absolute efficiency is defined as the ratio of the power of one diffraction order to the total transmitted/incident power. To demonstrate the universality of the presented design strategy, we have designed several OSMs with different bending angles. As shown in Figure S3 (Supporting Information), the diffraction efficiency is still higher than 90% for a large bending angle (–85°), which is almost impossible in traditional designs. More interestingly, the performance of those OSMs maintains well even at glancing incidence. These novel effects can be attributed to the employment of geometric phase principle, the implementation of iso-phase streamline optimization on streamlined structures, and the waveguiding effect of high-index dielectric structures.[41,42]

To highlight the superior performance of the OSM, we further compare it with the NSM, a quantized metasurface (QM), and a discrete metasurface (DM), as illustrated in **Figure 3**a, in terms of spectral and angular bandwidths (see Figures S4–S6 in the Supporting Information for their detailed results and geometrical shapes). To sufficiently sample the phase, both QM and DM adopt a 4-level phase quantization. We have optimized basic unit elements of the QM and DM to realize high polarization conversion efficiency at the design wavelength, under the condition that their minimum geometrical features are similar to that of the OSM. Note that the structural height of the QM is higher than that of the three others to realize high polarization conversion efficiency.

Figure 3b shows simulated-first-order diffraction efficiency spectra at normal incidence. The broadband property of the OSM was characterized by a tunable CO_2 laser at four different wavelengths ranging from 9.3 to 10.6 µm, which almost covers the entire wavelength band of our laser. Experimental results for different incident angles, displayed in Figure 3b and Figure S3 (Supporting Information), show a good agreement with simulations. To quantify spectral and angular bandwidths, average diffraction/absolute efficiencies (solid/dash curves, DEs/AEs) within 8–14 µm are depicted in Figure 3c as a function of the incident angle along the x-direction. Figure 3b,c indicates that the OSM outperforms the three others for both spectral and angular bandwidths. Furthermore, the superior performance of the OSM has also been demonstrated at oblique incidence along the y-direction (Figure S7, Supporting Information). The broadband and high diffraction efficiency of the OSM can be attributed to the specific dispersion characteristic of form-birefringence in silicon, which makes the local part of streamlined structures behave as a near-perfect achromatic half-wave plate in a

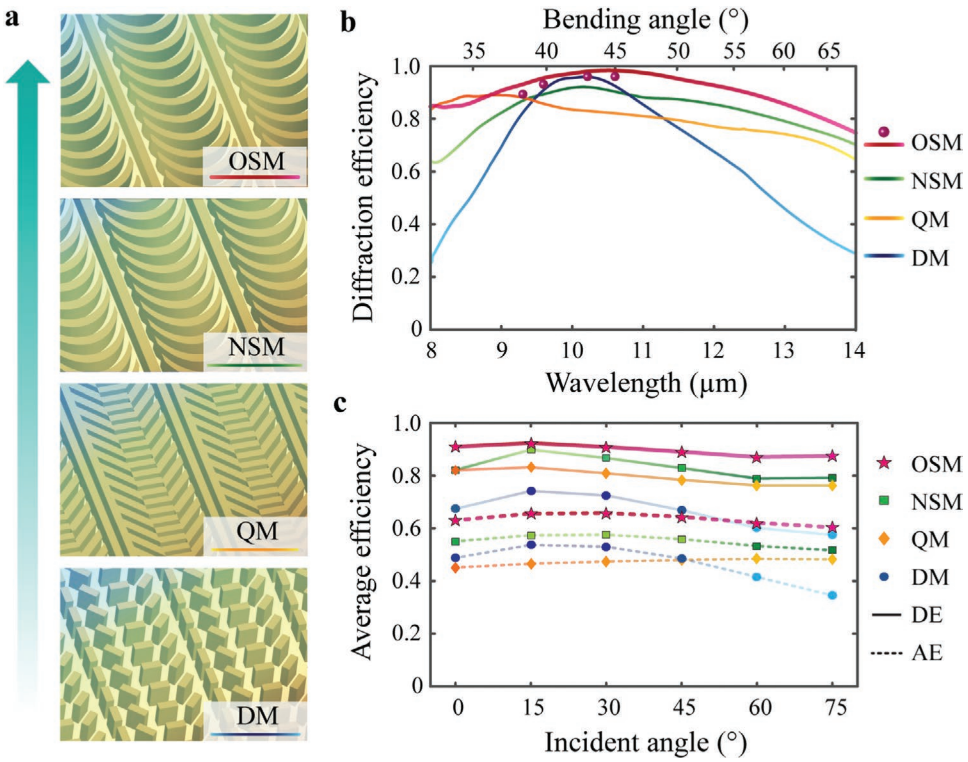

Figure 3. Comparison of four different subwavelength structures. a) Schematic illustrations of four different structures. The structural height of the DM is 7 µm, and others are 4.7 µm. b) Simulated-first-order diffraction efficiency spectra of four structures at normal incidence. The dots indicate measured-first-order diffraction efficiencies of the OSM. c) Simulated average diffraction/absolute efficiency (DE/AE) within 8–14 µm for different angles of incidence with respect to the *x*-direction. OSM: optimized streamlined metasurface; NSM: normal streamlined metasurface; QM: quantized metasurface; DM: discrete metasurface; DE: diffraction efficiency; AE: absolute efficiency.

wide spectral range.[43] However, this effect does not occur in discontinuous dielectric metasurfaces (QM and DM), which results in relatively narrow operating bandwidths.

4. Ultrawide-Angle Infrared Metalenses

As shown in **Figure 4**a, the metalens with a quadratic phase distribution can focus light rays emanating from different orientation angles on the same focal plane, $f = (\lambda_0/\lambda)f_0$, with a focus offset of $-(\lambda_0/\lambda)f_0 \sin\theta_i$ from the origin, where λ represents the incident wavelength and f_0 is the focal length at the design wavelength of λ_0 (see Section S4 in the Supporting Information for details). In this regard, the rotational symmetry of incidence can be perfectly converted to the translational symmetry of outgoing waves, leading to the broadband ultrawide-angle lensing performance.[46,47] Such a rapid phase gradient results in the fact that only part of light fields can contribute to the focal spot and others become evanescent after passing through the metalens, which can rarely be realized by discrete structures.

Since the proposed method for OSMs enables arbitrary continuous phase profile generation and ultrahigh diffraction efficiency, it provides a powerful framework for such wide-angle metalenses. As proof-of-concept demonstrations, we have designed, fabricated, and characterized two wide-angle streamlined metalenses (1D and 2D) with the same focal length of 5.12 mm and radius of 6 mm (see Sections S4 and S5 in the Supporting Information for details). These metalenses can focus left-handed CP light from the substrate into a tight spot. Here, we employed direct laser writing and inductive-coupled plasmonic etching to fabricate metalenses (see the Experimental Section in the Supporting Information for details). Besides, femtosecond-laser direct writing is a very suitable tool to make large-area and more complicated optical devices with the feature size at 1 µm.[48]

As shown in Figure S8 (Supporting Information), the measured focus offsets of both the two wide-angle metalenses agree well with the theoretical predictions from −88° to 88° at different wavelengths. Their corresponding coefficients of determination (R^2) are larger than 0.999. Significantly, the focal length remains the same with varied incident angles for a fixed wavelength, which facilitates spatial frequency measurement in the application of Fourier optics (Figure S9, Supporting Information).

According to the principle of reciprocity, the wide-angle metalens can be applied for laser beam steering directly, providing a promising candidate for lightweight and wide-angle lidar systems. Figure 4b shows the schematic illustration of the optical setup for laser beam scanning. A Fourier lens was utilized to focus the CP light at 10.6 µm wavelength on the focal plane of the 2D wide-angle metalens. The radiation direction can be readily tuned by horizontally moving the point source perpendicular to the optical axis with a distance of s_1,

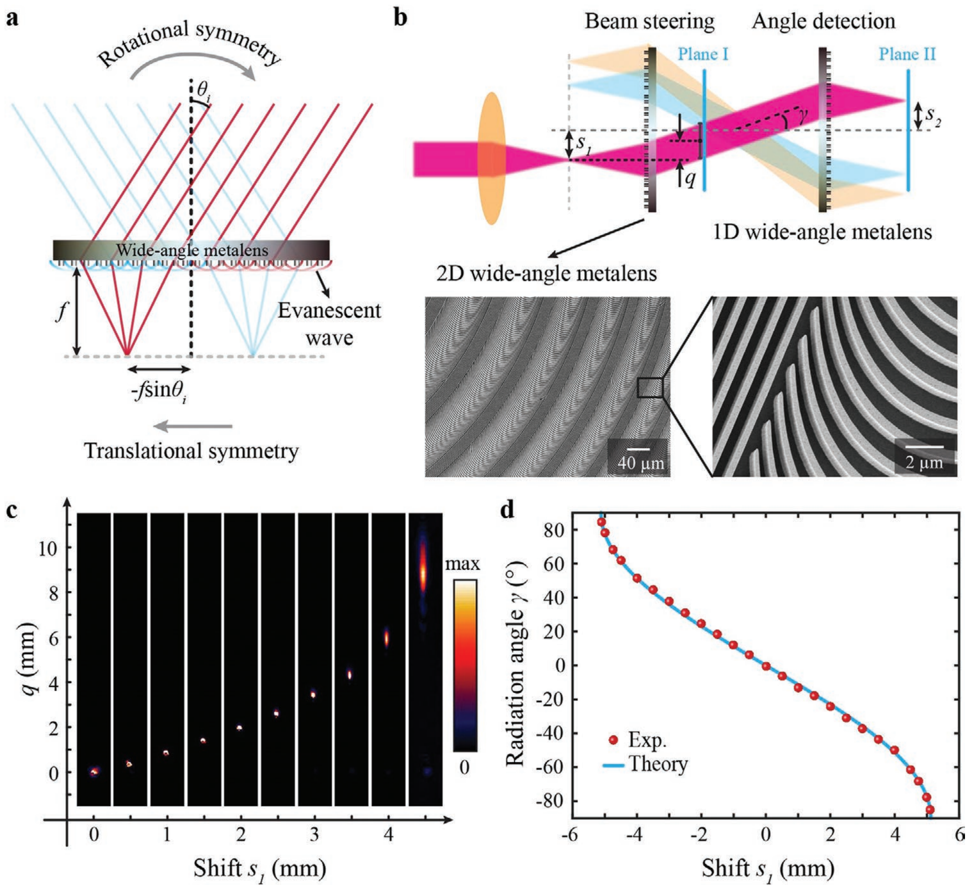

Figure 4. Wide-angle laser beam steering. a) Concept illustration of the symmetry conversion from rotational symmetry of incidence to translational symmetry of outgoing wave by the streamlined wide-angle metalens. b) Schematic illustration of the optical setup for both beam steering and radiation angle detection. Insets: SEM images of the 2D wide-angle metalens. c) Measured diffraction patterns for different shifts of the point source by placing the infrared detector on the plane I which is about 4.6 mm from the 2D wide-angle metalens. d) Measured radiation angles as a function of the point source shift.

corresponding to a radiation angle of $\gamma = -\sin^{-1}(s_1/f_0)$. Figure 4c sketches measured diffraction patterns that are captured by an infrared detector placed on the plane I in Figure 4b, showing the evolution of the radiation direction for different s_1. One can see that there is almost no noise or stray light. Due to the limited detection size of the infrared detector, we could not simultaneously capture the 0th-order and radiation beams when $|s_1| > 4.5$ mm (corresponding to $|\gamma| > 61.5°$). To detect the radiation angle, the 1D wide-angle metalens was employed and the infrared detector was placed on the focal plane of the 1D wide-angle metalens (plane II in Figure 4b). Please see Figure S11 (Supporting Information) for measured intensity distributions on plane II. The focus offset s_2 on its focal plane (as shown in Figure S11 in the Supporting Information) can be employed to measure the radiation angle by $-\sin^{-1}(s_2/f_0)$. Figure 4D shows measured radiation angles as a function of the shift of the point source, showing a good agreement with theoretical predictions ($R^2 > 0.999$), and an ultrawide radiation range from −85° to 85° has been experimentally demonstrated. The measured radiation efficiencies are shown in Figure S12 (Supporting Information).

We have designed a highly integrated long-wave infrared metacamera based on a wide-angle streamlined metalens (f_0 = 6.5 mm and R = 12.7 mm), an infrared detector, and an infrared band-pass filter (Figure S13, Supporting Information). To reduce energy losses by Fresnel reflection, antireflection structures were fabricated on the other side of the metalens substrate and the transmission was improved by ≈25% (Figure S14, Supporting Information). Considering these superior properties of high efficiency, spin sensitivity, angular insensitivity, and compact size, large-FOV chiral thermal imaging can be achieved (**Figure 5**a). As shown in Figure 5b, the metacamera can be directly used for human thermal imaging, even if a narrow-band filter is embedded, which proves the high-efficiency and wide-angle capability. Although the signal-to-noise ratio is worsened by its strong thermal noise (the infrared detector is uncooled), the body contour and gesture can be clearly captured, and the imaging resolution of the metacamera can reach the cut-off spatial frequency of our infrared detector (29.41 lp mm^{-1}; Figure S15, Supporting Information). Subsequently, the chiral detection ability of the metacamera, which may find versatile applications ranging from environmental sensing to biological studies,[20] was demonstrated by employing a circular asymmetric transmission device in our previous work[6] as a chiral target. Figure 5c,d shows its two images when the radiation source from a heating ceramic lamp is illuminating from two sides after passing through a linear

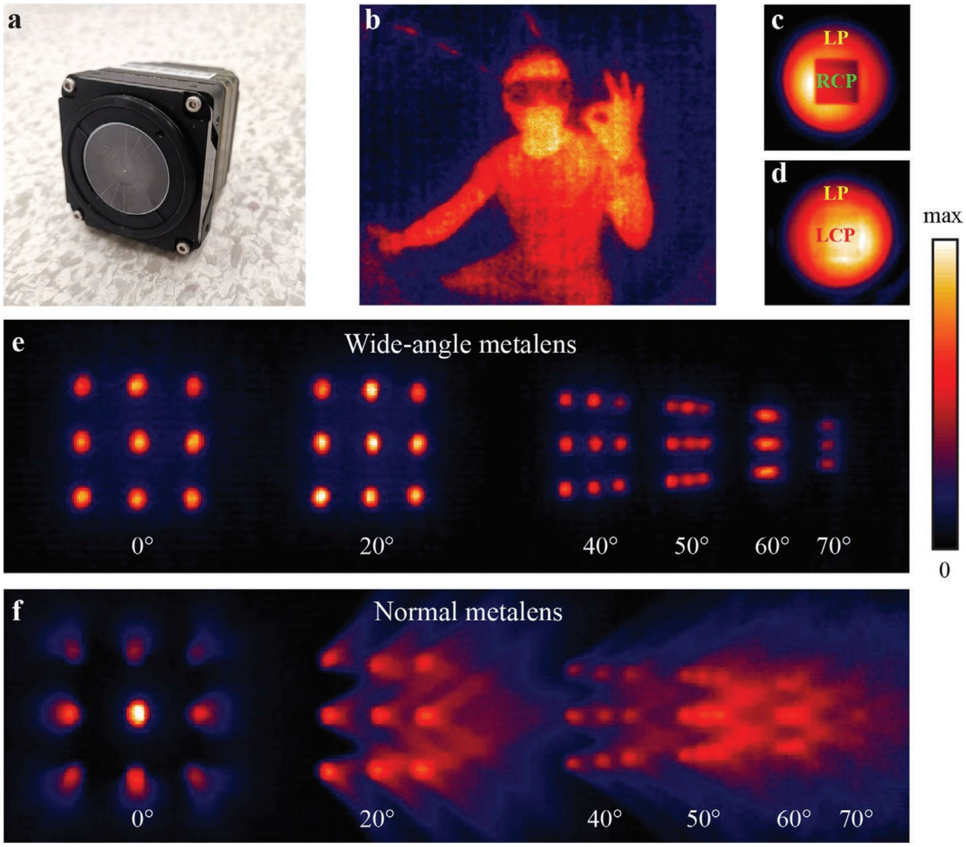

Figure 5. Large-FOV chiral thermal imaging. a) Photograph of the highly integrated long-wave infrared metacamera. b) A human thermal image formed by the metacamera at a distance of ≈60 cm. c,d) Two images of a circular asymmetric transmission device formed by the metacamera for forward and backward propagation. e,f) Images of a 3 × 3 array of lamps at different half-FOVs formed by wide-angle and normal metalenses. These two metalenses have the same focal length and radius, and the objective distance is ≈200 cm.

polarizer, showing an obvious difference in brightness owing to the strong chiral response of the metacamera. Finally, a large FOV has been experimentally demonstrated by horizontally moving a 3 × 3 array of lamps (Figure S16, Supporting Information) perpendicular to the optical axis. As shown in Figure 5e, the designed wide-angle metalens can image the lamps clearly in a large FOV. By contrast, restricted by the strong coma aberration of the normal metalens with a phase profile of $\phi(r) = -k_0(r^2 + f_0^2)^{1/2}$, merely the lamp on the optical axis can be clearly imaged.

To further demonstrate the generality of isophase streamline optimization, a near-infrared metacamera was designed aiming at the wavelength of 940 nm (**Figure 6**a), in which a streamlined metalens was fabricated through a silicon-on-sapphire wafer (see the Experimental Section in the Supporting Information for details). As can be seen from its modulation transfer function (Figure 6b), diffraction-limited imaging can be realized within 178° FOV by adding an aperture stop at the front of the metalens.[49] The phase distribution of the metalens was optimized based on the ray tracing method in Zemax. Owing to the single-chip planar design, it is extremely hard to make all light rays intersect in the Airy disk. For example, a small part of light rays at the 30° half-FOV are outside the Airy disk, which makes its spot profile look somewhat bigger than that at the 60° half-FOV. Nevertheless, their modulation transfer function (MTF) is still very close to the diffraction limit, as MTF was utilized as the figure of merit. Furthermore, when optimizing the phase profile of metalenses, one can enhance the weight of one FOV to further improve its MTF and decrease its spot profile. Owing to its high efficiency and strong angular robustness (Figure 6c), ultralarge-FOV imaging can be realized under the illumination of a normal near-infrared LED source (Figure 6d), with a band-pass filter (940 ± 5 nm) incorporated in front of the sensor. Besides nocturnal active imaging, this metacamera can also be directly applied for daytime passive imaging (Figure S17, Supporting Information). These results mean that such a metacamera is already practical for night vision, spectral imaging, 3D imaging, etc.

5. Conclusion

We have proposed a streamlined metasurface platform to generate arbitrary near-perfect phase distributions. Owing to optimized continuous structures, spurious diffraction orders are efficiently suppressed in a wide spectral and angular range, resulting in the maximum diffraction efficiency approaching 100%. Moreover, it has been demonstrated that the presented metasurfaces obviously outperform their discrete counterparts

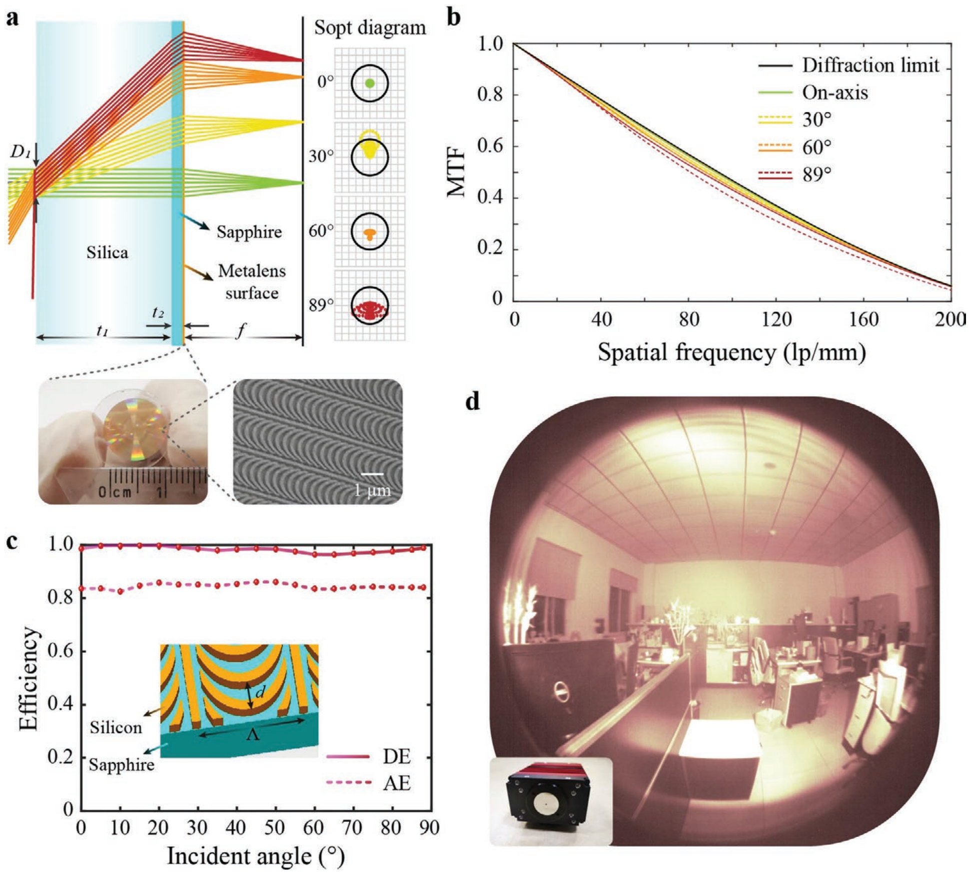

Figure 6. Demonstration of a near-infrared diffraction-limited large-FOV metacamera. a) Optical layout with $t_1 = 4.99$ mm, $t_2 = 0.45$ mm, $f = 4.48$ mm, and $D_1 = 1$ mm. The insets on the right show spot diagrams for 0°, 30°, 60°, and 89° incidence, and the black circles indicate an Airy disk. Insets at the bottom: Optical and SEM images of a fabricated wide-angle metalens with a diameter of 12 mm. b) Optical MTF for different half-FOVs (dashed curves: tangential MTF; solid curves: sagittal MTF). c) Diffraction/absolute efficiency (DE/AE) at the wavelength of 940 nm for different incident angles, showing strong angular robustness. The inset shows the model for simulations with $\Lambda = 940/\sin(45°)$ nm, $d = 350$ nm, and the structural height being 350 nm. d) An indoor image formed by the near-infrared metacamera. Inset: imaging setup. The pixel size of the employed detector (Applied Vision, GT2050NIR) is 5.5 µm × 5.5 µm.

in both spectral and angular bandwidths. To the best of our knowledge, this is the first report on the simultaneous realization of broadband, high-efficiency, and ultrawide-angle wavefront control for single-chip planar optical elements. We demonstrated its application prospects in infrared polarization imaging and laser beam scanning, possessing the largest known diffraction-limited FOV (178°) for single-chip planar devices. The presented infrared streamlined metalenses, with compact size, polarization sensitivity, ultralarge FOV, and minimal thermal sensitivity, are of great significance in the vision systems of thermal/night-vision imagers, unmanned vehicles, onboard planes or satellites, and so forth.

With further global optimization based on the geometric database, a higher efficiency over 99% within a wide wavelength range is foreseeable. Such efficiency is comparable to that of low-index liquid crystal devices which operate within a narrower angular range.[50] Owing to its ultrahigh diffraction efficiency, the proposed streamlined metasurfaces will provide a powerful tool for designing multilayer cascaded optical systems, enabling more powerful functionalities not available with a single metasurface. For example, the effective aperture of wide-angle metalenses could be increased through multilayer streamlined structures,[51] which can improve the angular resolution of the metalens and enhance the detection ability of weak-intensity targets. Therefore, this work can provide a general platform for constructing many high-performance functional devices and systems.

6. Experimental Section

The Experimental Section is presented in Section S5 of the Supporting Information.

Supporting Information

Supporting Information is available from the Wiley Online Library or from the author.

Acknowledgements

F.Z. and M.P. contributed equally to this work. This work was supported by the National Natural Science Foundation of China (No. 61975210, U20A20217, and 61875202) and Project funded by China Postdoctoral Science Foundation (No. 2020M680153). F. Zhang would like to thank Dr. M. Xu for revising the manuscript and Dr. J. Jin for discussing experiments. All authors thank all medical workers and volunteers around the world for their efforts to fight the COVID-19 virus.

Conflict of Interest

The authors declare no conflict of interest.

Data Availability Statement

The data that support the findings of this study are available from the corresponding author upon reasonable request.

Keywords

catenary optics, metasurfaces, streamlined structures, wide-angle imaging

Received: December 3, 2020
Revised: December 28, 2020
Published online: February 10, 2021

[1] C. L. Tan, H. Mohseni, *Nanophotonics* **2018**, *7*, 169.
[2] H. Liang, A. Martins, B.-H. V. Borges, J. Zhou, E. R. Martins, J. Li, T. F. Krauss, *Optica* **2019**, *6*, 1461.
[3] W. Liu, H. Cheng, J. Tian, S. Chen, *Adv. Phys.: X* **2020**, *5*, 1742584.
[4] X. Luo, *Sci. China: Phys., Mech. Astron.* **2015**, *58*, 594201.
[5] N. Yu, P. Genevet, M. A. Kats, F. Aieta, J.-P. Tetienne, F. Capasso, Z. Gaburro, *Science* **2011**, *334*, 333.
[6] F. Zhang, M. Pu, X. Li, P. Gao, X. Ma, J. Luo, H. Yu, X. Luo, *Adv. Funct. Mater.* **2017**, *27*, 1704295.
[7] L. Jin, Y.-W. Huang, Z. Jin, R. C. Devlin, Z. Dong, S. Mei, M. Jiang, W. T. Chen, Z. Wei, H. Liu, J. Teng, A. Danner, X. Li, S. Xiao, S. Zhang, C. Yu, J. K. W. Yang, F. Capasso, C.-W. Qiu, *Nat. Commun.* **2019**, *10*, 4789.
[8] F. Zhang, Y. Guo, M. Pu, X. Li, X. Ma, X. Luo, *Opto-Electron. Eng.* **2020**, *47*, 200366.
[9] W. T. Chen, A. Y. Zhu, V. Sanjeev, M. Khorasaninejad, Z. Shi, E. Lee, F. Capasso, *Nat. Nanotechnol.* **2018**, *13*, 220.
[10] S. Wang, P. C. Wu, V. C. Su, Y. C. Lai, M. K. Chen, H. Y. Kuo, B. H. Chen, Y. H. Chen, T. T. Huang, J. H. Wang, R. M. Lin, C. H. Kuan, T. Li, Z. Wang, S. Zhu, D. P. Tsai, *Nat. Nanotechnol.* **2018**, *13*, 227.
[11] X. Li, L. Chen, Y. Li, X. Zhang, M. Pu, Z. Zhao, X. Ma, Y. Wang, M. Hong, X. Luo, *Sci. Adv.* **2016**, *2*, e1601102.
[12] X. Fang, H. Ren, M. Gu, *Nat. Photonics* **2020**, *14*, 102.
[13] C. Qian, B. Zheng, Y. Shen, L. Jing, E. Li, L. Shen, H. Chen, *Nat. Photonics* **2020**, *14*, 383.
[14] X. Ni, Z. J. Wong, M. Mrejen, Y. Wang, X. Zhang, *Science* **2015**, *349*, 1310.
[15] P. Huo, C. Zhang, W. Zhu, M. Liu, S. Zhang, S. Zhang, L. Chen, H. J. Lezec, A. Agrawal, Y. Lu, T. Xu, *Nano Lett.* **2020**, *20*, 2791.
[16] Y. Zhou, H. Zheng, I. I. Kravchenko, J. Valentine, *Nat. Photonics* **2020**, *14*, 316.
[17] S. Sun, Q. He, S. Xiao, Q. Xu, X. Li, L. Zhou, *Nat. Mater.* **2012**, *11*, 426.
[18] X. Zhang, Q. Xu, Q. Li, Y. Xu, J. Gu, Z. Tian, C. Ouyang, Y. Liu, S. Zhang, X. Zhang, J. Han, W. Zhang, *Sci. Adv.* **2016**, *2*, e1501142.
[19] L. Li, K. Yao, Z. Wang, Y. Liu, *Laser Photonics Rev.* **2020**, *14*, 1900244.
[20] N. A. Rubin, G. D'Aversa, P. Chevalier, Z. Shi, W. T. Chen, F. Capasso, *Science* **2019**, *365*, eaax1839.
[21] S. Chen, W. Liu, Z. Li, H. Cheng, J. Tian, *Adv. Mater.* **2020**, *32*, 1805912.
[22] X. Ma, M. Pu, X. Li, Y. Guo, X. Luo, *Opto-Electron. Adv.* **2019**, *2*, 180023.
[23] F. Zhang, X. Xie, M. Pu, Y. Guo, X. Ma, X. Li, J. Luo, Q. He, H. Yu, X. Luo, *Adv. Mater.* **2020**, *32*, 1908194.
[24] C. Yan, X. Li, M. Pu, X. Ma, F. Zhang, P. Gao, K. Liu, X. Luo, *Appl. Phys. Lett.* **2019**, *114*, 161904.
[25] M. Pu, X. Li, X. Ma, Y. Wang, Z. Zhao, C. Wang, C. Hu, P. Gao, C. Huang, H. Ren, X. Li, F. Qin, J. Yang, M. Gu, M. Hong, X. Luo, *Sci. Adv.* **2015**, *1*, e1500396.
[26] X. Luo, *Engineering Optics 2.0: A Revolution in Optical Theories, Materials, Devices and Systems*, Springer, Berlin, Germany **2019**.
[27] N. Yu, F. Capasso, *Nat. Mater.* **2014**, *13*, 139.
[28] W. T. Chen, A. Y. Zhu, F. Capasso, *Nat. Rev. Mater.* **2020**, *5*, 604.
[29] X. Luo, *Adv. Mater.* **2019**, *31*, 1804680.
[30] X. Luo, *Catenary Optics*, Springer, Berlin, Germany **2019**.
[31] P. Lalanne, P. Chavel, *Laser Photonics Rev.* **2017**, *11*, 1600295.
[32] C. J. Bouwkamp, *Rep. Prog. Phys.* **1954**, *17*, 35.
[33] P. Lalanne, S. Astilean, P. Chavel, E. Cambril, H. Launois, *J. Opt. Soc. Am. A* **1999**, *16*, 1143.
[34] M. Khorasaninejad, W. T. Chen, R. C. Devlin, J. Oh, A. Y. Zhu, F. Capasso, *Science* **2016**, *352*, 1190.
[35] X. Luo, M. Pu, X. Li, X. Ma, *Light: Sci. Appl.* **2017**, *6*, e16276.
[36] X. Zhang, G. Liang, D. Feng, L. Zhou, Y. Guo, *J. Phys. D: Appl. Phys.* **2019**, *53*, 104002.
[37] D. Wang, Y. Hwang, Y. Dai, G. Si, S. Wei, D. Y. Choi, D. E. Gomez, A. Mitchell, J. Lin, X. Yuan, *Small* **2019**, *15*, 1900483.
[38] T. Phan, D. Sell, E. W. Wang, S. Doshay, K. Edee, J. Yang, J. A. Fan, *Light Sci.: Appl.* **2019**, *8*, 48.
[39] Z. Lin, S. G. Johnson, *Opt. Express* **2019**, *27*, 32445.
[40] D. Sell, J. Yang, S. Doshay, R. Yang, J. A. Fan, *Nano Lett.* **2017**, *17*, 3752.
[41] P. Lalanne, *J. Opt. Soc. Am. A* **1999**, *16*, 2517.
[42] J. Yang, J. A. Fan, *Opt. Express* **2017**, *25*, 23899.
[43] H. Kikuta, Y. Ohira, K. Iwata, *Appl. Opt.* **1997**, *36*, 1566.
[44] F. Zhang, M. Pu, J. Luo, H. Yu, X. Luo, *Opto-Electron. Eng.* **2017**, *44*, 319.
[45] X. Luo, M. Pu, Y. Guo, X. Li, F. Zhang, X. Ma, *Adv. Opt. Mater.* **2020**, *8*, 2001194.
[46] M. Pu, X. Li, Y. Guo, X. Ma, X. Luo, *Opt. Express* **2017**, *25*, 31471.
[47] A. Martins, K. Li, J. Li, H. Liang, D. Conteduca, B.-H. V. Borges, T. F. Krauss, E. R. Martins, *ACS Photonics* **2020**, *7*, 2073.
[48] J. Yuechen, W. Shixiang, C. Feng, *Opto-Electron. Adv.* **2020**, *3*, 190042.
[49] J. Engelberg, C. Zhou, N. Mazurski, J. Bar-David, A. Kristensen, U. Levy, *Nanophotonics* **2020**, *9*, 361.
[50] C. Oh, M. J. Escuti, *Opt. Lett.* **2008**, *33*, 2287.
[51] B. Groever, W. T. Chen, F. Capasso, *Nano Lett.* **2017**, *17*, 4902.